Experimental Mechanics (2018) 58:269–282
DOI 10.1007/s11340-017-0341-8

Thermography Applied to the Study of Fatigue Crack Propagation in Polycarbonate

R.B. Vieira[1] · **G.L.G Gonzáles**[1] · **J.L.F. Freire**[1]

Received: 6 February 2017 / Accepted: 27 September 2017 / Published online: 5 October 2017

Abstract Thermography was used to study the propagation of fatigue cracks during cyclic loading of pre-cracked SAE keyhole polycarbonate specimens. A micro-bolometer infrared camera (FLIR A655sc) and a commercially available software program (DeltaTherm2) were employed. The stress intensity factors were determined using a hybrid thermoelastic stress analysis (TSA) technique. The crack growth rate was determined via thermography using two different approaches. The first approach used the output of the crack-tip position from the developed TSA algorithm and the number of cycles between data sets. The second approach used temperature measurement as a new way to determine da/dN (crack growth rate) directly. As a result, da/dN vs ΔK (stress intensity factor range) graphs were plotted and fitted using Paris' law. A comparison between the resultant da/dN vs ΔK curves and results found in the literature, as well as curves from the finite element method (FEM) simulations showed good agreement. The conclusion was that thermography is a very powerful tool that can detect, measure and monitor fatigue cracks in polycarbonate.

✉ R. B. Vieira
renato.bicharav@hotmail.com

G. L. G Gonzáles
giancarlo.g.gonzales@outlook.com

J. L. F. Freire
jlfreire@puc-rio.br

[1] Department of Mechanical Engineering, Pontifical Catholic University of Rio de Janeiro (PUC-Rio), Rio de Janeiro 22451-900, Brazil

Keywords Thermoelasticity · Fatigue · Crack propagation · Polycarbonate · Stress intensity factor · Paris' law · Digital image correlation · Finite elements

Introduction

Polycarbonate (PC) is a polymer having high temperature resistance, high ductility and high mechanical and impact strengths when compared to other engineering plastics. These properties make polycarbonate the normal choice for engineering applications in the civil, automotive and aeronautical industries, as well as the frequent choice for relatively high stress applications. Considering that cyclic loading is bound to happen in most of these applications, studying the fatigue properties of such a material is of utmost importance. Although it presents high transparency in the visible spectrum, polycarbonate is virtually opaque to infrared radiation, absorbing and emitting most of it. This property makes polycarbonate a good choice for infrared applications.

The present paper reports results from a line of investigation [1, 2] that puts together the study of fatigue crack initiation and propagation in annealed polycarbonate with temperature measurements taken with a micro-bolometer infrared camera. The thermographic temperature measurements were used to directly infer the fatigue response (crack initiation and crack propagation) of specific tested specimens, as well as to determine fracture mechanics stress intensity factors (SIF) of the propagating cracks using the Thermoelasticity Stress Analysis (TSA) technique [3–13]. Two resultant outcomes will be presented and discussed herein: fatigue propagation of a crack with length (a) per loading cycle (da/dN), and SIF range (ΔK) determination. Combining these two outcomes enables determining the so-called Paris' crack propagation exponential law ($da/dN = C.\ \Delta K^p$), C and p resulting from

the exponential fitting using the least square method, in annealed polycarbonate.

Fatigue crack initiation and propagation in specimens of annealed polycarbonate were studied in [1], where a survey of the literature on both subjects was presented. References [14–19] summarize the extraction of a number of relevant findings. In what concerns crack propagation in polycarbonate, Hertzberg et al. [14] concluded that the use of classical fracture mechanics concepts, such as the stress intensity factor (SIF) and Paris' Law, was appropriate for polycarbonate. Corroborated by Hertzberg et al. [16], Gerberich et al. [15] investigated the effects of temperature on crack growth in polycarbonate specimens. Ward et al. [17] studied the effect of specimen thickness on crack growth rates in polycarbonate specimens. Pruitt et al. [18] also explored the effects of specimen thickness, as well as the effects of stress or load ratio (R = minimum stress (σmin) /maximum stress (σmax)) in one cycle of fatigue behavior in polycarbonate. Using Crack Layer theory to successfully predict crack growth rates, Moet et al. [19] investigated the effect of yielding mechanisms on fatigue crack growth in polycarbonate. However, a search of the literature revealed that no study has yet applied infrared thermography to fatigue in polycarbonate. Therefore, this paper makes full use of thermographic techniques to explore fatigue behavior in polycarbonate.

Thermoelasticity (TSA) is a non-contact, full-field stress measurement technique based on the thermoelastic effect [3]. By using infrared thermography, it is possible to measure the temperature distribution on the surface of a cyclically deforming body. This distribution can then be correlated with the stress range acting at each point. Eq. 1 describes how temperature measurements are converted into stress data in practical TSA applications.

$$\Delta(\sigma_1 + \sigma_2) = A\,S \tag{1}$$

where $\Delta\sigma_1$ and $\Delta\sigma_2$ are the principal stress ranges, S is the thermoelastic signal from the TSA software (proportional to the temperature variation caused by the loading), and A is the thermoelastic coefficient, related to the material's properties and to the thermographic setup.

Thermography, especially TSA, has been used on occasion to analyze the stress distribution around fatigue cracks in order to determine stress intensity factors. Stanley and Chan [5] used the first two terms of Westergaard's stress function to fit the thermoelastic data around cracks in mode I and II. Stanley and Dulieu-Smith [6] based their approach on the cardioid format of the isopachic fringes around a crack tip. Lesniak et al. [7] used Williams' asymptotic stress field equations to fit the thermal data by using the least squares method (LSM), whereas Lin et al. [8] approached the problem using the J-integral formulation in the data fitting process. Tomlinson et al. [9] developed a technique based on Muskhelishvili's stress field equations and a multipoint-over-deterministic method (MPODM). Díaz et al. [10, 11] proposed a methodology for finding the crack tip position by looking at the thermoelastic data, and then fitting the data using a non-linear approach in order to measure SIFs of propagating cracks. Marsavina et al. [12] used TSA to investigate crack closure during fatigue, and Tomlinson and Olden [13] presented a broad review of the use of TSA in fracture mechanics and fatigue cracks. The present work uses an algorithm based on Westergaard's solution for the stress field near the crack tip, in combination with experimental results from TSA, in order to determine stress intensity factors. Finite element simulations were conducted to calculate theoretical SIFs as a means for comparing and verifying the results.

The study outlined in the following sections consisted of two main approaches for determining the Paris' law crack propagation in annealed polycarbonate specimens. The first approach used the SIF algorithm to find the ΔK and da/dN values (since one of the outputs of the non-linear algorithm is the crack tip position). In this procedure, TSA is the only tool used and therefore it can be implemented to automatically determine the crack propagation law. Although polycarbonate was used, this approach can also be applied to other materials that follow Paris' law. The second approach used the thermographic temperature measurements at the propagating crack tip to innovatively find the value of da/dN and then combine these results with SIFs values. In this approach these SIF values were determined via TSA and also via the Finite Element Method (FEM) for comparison purposes. The next section summarizes experimental details regarding specimen preparation, material calibration, and infrared camera. Then, the following section presents a thorough discussion of the SIF, crack-tip localization and da/dN determination algorithms. The section after that shows the empirical relationship between crack propagation and temperature measurements. It is based on an extension of the Thermographic or Risitano's method [20, 21], used to measure the fatigue limit and stress vs the number of fatigue curve cycles (S-N). Then a section on Results and Discussion follows, comparing crack propagation according to Paris' law using the two approaches with results found in the literature. The paper's conclusions are presented in the last section.

Experimental Procedures

Thermoelastic Coefficient Calibration

In order to obtain the value of A for a specific material and setup, a calibration experiment must be conducted. There are different approaches to this process [4]. In the present work, the calibration test consisted of a dog-bone specimen, with known dimensions (machined from the same polycarbonate sheet as the cracked specimens and having the same surface

texture), being cyclically loaded in uniaxial tension, as shown in Fig. 1. Then, the resultant stress ranges and measured thermoelastic signals were used to calculate the value of A. For the ambient temperature, material and setup used here, the coefficient was determined to be A = 1.12 MPa/Cam units ("Cam unit" is used as the unit of the thermoelastic signal from the TSA software).

Specimen Preparation

SAE keyhole specimens were machined from a single polycarbonate sheet (thickness = 3.9 mm), all taken at the same orientation. Some residual stresses from manufacturing the sheet, as well as from the machining processes, were present [1]. In order to eliminate the influence from these residual stresses, a specific heat treatment was applied to the specimens, heating them up to 160 °C in a span of 4 h. The temperature was then kept constant for 6 h, after which the specimens were cooled down to the ambient temperature in another 4 h. A photoelastic analysis (using a transmission polariscope) confirmed that birefringence caused by the residual stresses was eliminated after the heat treatment [1].

Specimen Pre-Cracking

In order to nucleate a crack and propagate it to an initial crack length (a), the specimens were cyclically loaded using the pneumatic machine shown in Fig. 1. Loading was controlled using a load cell (5000 N) connected in series with the specimen and the pneumatic muscle, which sent the signal to the servo-valve. The frequency used for all tests was 5 Hz, and the magnitude was manually controlled using a valve that regulated the air pressure entering the muscle (load amplitude of 225 N ± 1 N and R = (Min load/Max load) = 0.3 for pre-cracking).

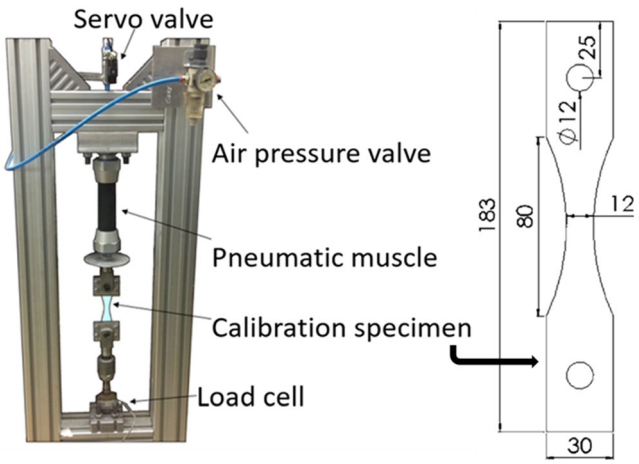

Fig. 1 Cyclic pneumatic machine and calibration tensile specimen (dimensions in mm); specimen thickness = 3.9 mm

The specimen dimensions after the pre-cracking process are shown in Fig. 2.

Infrared Imaging

The infrared camera used for the experiment was the FLIR A655sc. It has a focal plane array detector composed of 640 × 480 uncooled micro-bolometers and can record full-frame data at up to 50 Hz. It has a spatial resolution of 17 μm and a sensitivity of 30 mK. Micro-bolometer infrared cameras are a less expensive alternative to the cooled quantum detectors used by most other authors [22].

There were two software programs used in combination with the infrared camera in order to accomplish the measurements required for the study. When making direct temperature measurements, the ResearchIR software program from FLIR was used.

For the TSA tests, DeltaTherm2, a software program from Stress Photonics Inc., was used to convert the temperature data into TSA data. Typically, the TSA technique requires a lock-in process, which correlates the ΔT data with a reference signal, usually obtained from the function generator that feeds the cyclic actuator. DeltaTherm2 automates this process and takes the reference signal directly from the ΔT measurements, making the whole TSA test much simpler to set up and, therefore, making possible the use of less expensive cameras that do not have the lock-in capability.

For most thermography applications, including TSA, it is advisable to prepare the specimen in a way that maximizes infrared emissivity. This is usually accomplished by painting the surface with matt black paint. Nonetheless, polycarbonate has a naturally high infrared emissivity (ε = 0.9), which made it a very suitable material for this study, since it is transparent to visible light while being "opaque" to the infrared spectrum [23].

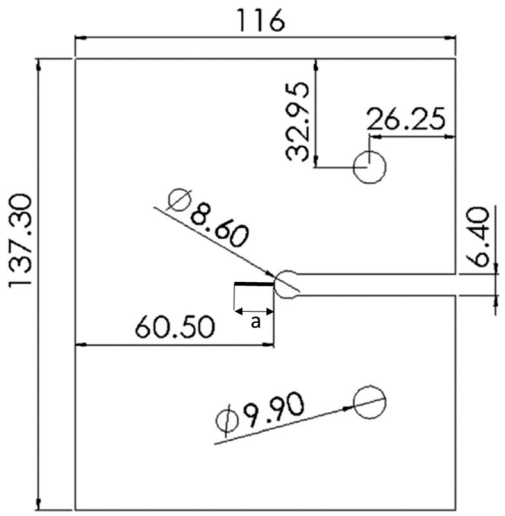

Fig. 2 Key-hole fatigue specimen (dimensions in mm)

Stress Intensity Factor Algorithm

TSA results can be understood as a complex variable, consisting of a magnitude, which is proportional to the temperature variation caused by the thermoelastic effect, and a phase angle, which is related to the signal of the stresses acting at a particular point. Figure 3 shows the typical magnitude and phase results obtained by cyclically loading the polycarbonate specimens. Figure 3(a) shows the magnitude map, while Fig. 3(b) shows the phase angle map around a crack with length a = 10 mm. It is obvious that the stresses concentrated at the crack tip cause a much higher temperature variation there.

Figure 4 shows a flowchart outlining how the algorithm for stress intensity factor calculation works, including its inputs and outputs. From the TSA magnitude and phase data, it is possible to generate corrected TSA data (with the compressive parts of the stresses converted to negative magnitude):

$$S = \begin{cases} Mag\ if\ |phase| < 45^o \\ -Mag\ if\ |phase| > 45^o \end{cases} \quad (2)$$

where S is the corrected TSA data, Mag is the magnitude data value in "camera units," and |phase| is the absolute value of the phase angle, in degrees.

One other input required for the procedure is the mathematical model that is being used. In this case, a Westergaard stress function (We) was used to describe the stress field around the crack tip

$$We(x,y) = \sigma_1 + \sigma_2 = 2[Re(Z) + Re(Z)] \quad (3)$$

with

$$Z = \sum_{n=0}^{N} [A_n z^{n-0.5}]$$
$$Y = \sum_{m=0}^{M} B_m z^m \quad (4)$$

where N and M determine the number of coefficients to be used (usually 2 to 4 in the present paper), A_n and B_m are the data fitting coefficients, and z is the complex variable of the point coordinates:

$$z = (x - x_o) + i(y - y_o) \quad (5)$$

where x and y are the horizontal and vertical coordinates of a point (placing the origin at the estimated crack tip location with the x axis pointing in the direction of the crack growth and the y axis pointing up), and $i = \sqrt{-1}$. Parameters x_o and y_o represent the unknown crack tip positioning errors in the horizontal and vertical directions. Next, there are two approaches, either $x_o = y_o = 0$, (i.e. the crack tip is determined assuming no error, making the problem linear), or the error values must be solved for during the optimization process, making the problem non-linear. Both approaches are used in this paper.

The final required inputs are the spatial resolution (SR) and the TSA calibration factor (A). The spatial resolution is easily determined via a known dimension in the specimen,

$$SR = {}^{W}/_{p} \quad (6)$$

where SR is the spatial resolution in mm/pixel, W is a known dimension of the specimen in mm (i.e. width), and p is the number of pixels the dimension measures on the thermographic image. The calibration factor (A) is determined as described above, using a calibration experiment. Nominal pixel size for the TSA experiments was 0.2 mm.

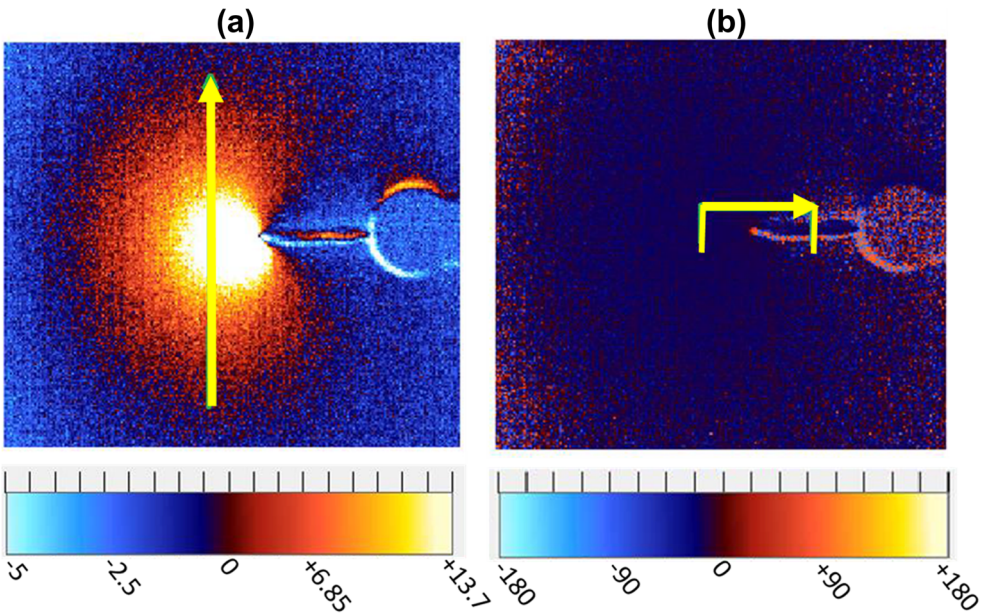

Fig. 3 (**a**) Magnitude (cam units) and (**b**) Phase angle map (degrees) around a crack with length a = 10 mm

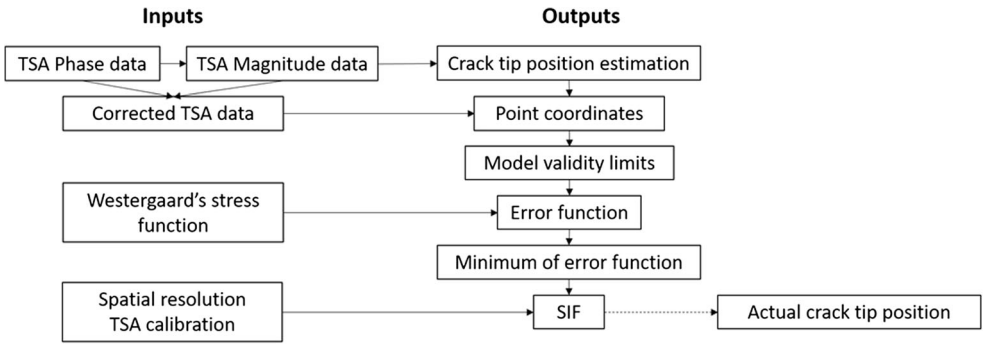

Fig. 4 SIF algorithm flowchart

Stress Intensity Factor Algorithm – Crack Tip Estimation

This work uses a specially improved, automated version of the methodology proposed in [10] to estimate the position of the crack tip. First, the image needs to be positioned so that the crack is horizontal. Then, using the TSA magnitude map, the vertical position of the crack tip (Y_o') is estimated by plotting y vs $1/S^2$ curves for each vertical line in the image (perpendicular to the crack, as shown by the vertical arrow in Fig. 3(a). The resulting graphs, for the lines in front of the crack tip, have a clear $1/S^2$ minimum value. The mean value of y where this minimum value occurs for all the vertical lines is equal to Y_o'. Figure 5(a) shows a typical y vs $1/S^2$ plot.

The horizontal position of the crack tip (X_o') is estimated using what is called the phase shift. Due to the very short plasticity area near the crack tip and the subsequent opened crack, the adiabatic conditions required by TSA are lost. This can be seen as an abrupt change in the phase angle directly in front of the crack tip. In the horizontal phase vs x curve at Y_o' (along the direction indicated by the horizontal arrow in Fig. 3(b), the position where this abrupt change occurs is equal to X_o'. Figure 5(b) shows a typical phase vs x plot.

Having determined the values of X_o' and Y_o', the coordinates assignment step is simple: each point of the image gets assigned to an x and a y value, which are the horizontal and vertical distances from the estimated crack tip, respectively.

Stress Intensity Factor Algorithm – Model Validity Limits Verification

The points used for the data fitting process must be in accordance with the mathematical model. In [11], the authors concluded that the model predicts a linear behavior of $1/S^2$ with respect to the distance from the crack tip. They proposed that only the points of Fig. 5(a) that presented a linear behavior should be used in the data fitting process.

The methodology used in the present work uses the same argument, but instead of using the vertical line plots, it uses plots of $1/S^2$ vs r, where r is the radial distance from the estimated crack tip. With r and θ being the polar coordinates centered at X_o' and Y_o', and θ = 0 being the horizontal line ahead of the crack, $1/S^2$ vs r curves are plotted for each 1 degree increment of θ between -120° and +120°, totaling

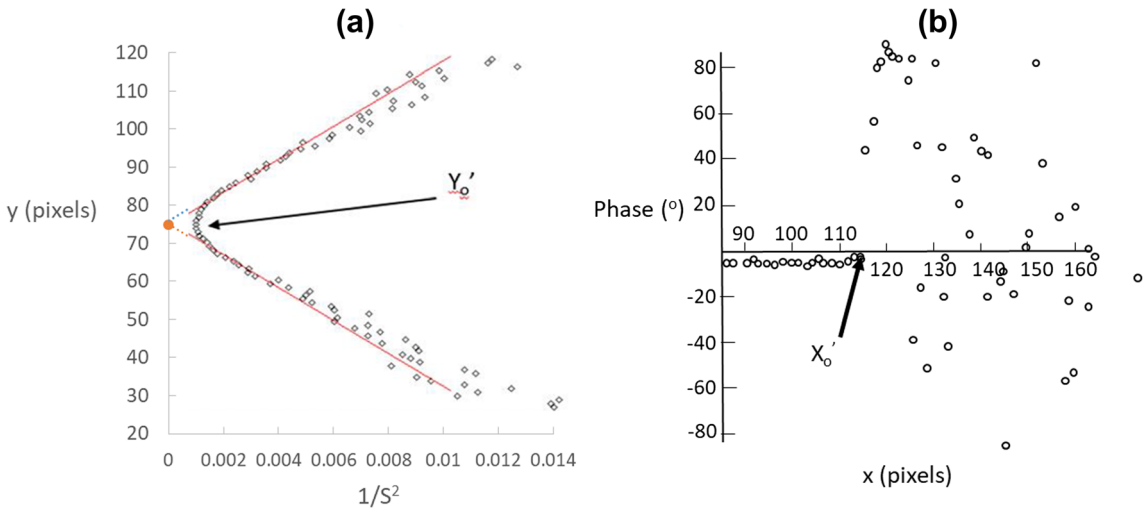

Fig. 5 (**a**) Typical y vs $1/S^2$ plot. (**b**) Typical phase vs x plot

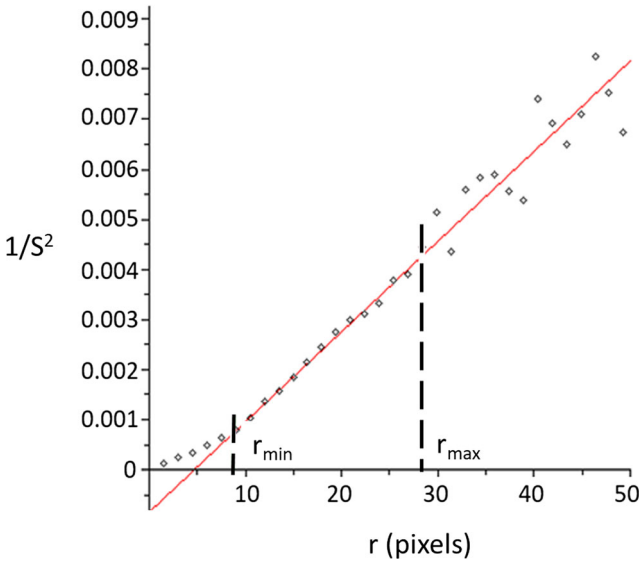

Fig. 6 Typical $1/S^2$ vs r plot

241 curve plots. Figure 6 shows an example of one of these plots.

For each of the $1/S^2$ vs r plots, r_{min} and r_{max} values were determined using two margins of tolerance of non-linearity, which were manually adjusted to fit the data. The authors verified that the r_{min} value for each analyzed $1/S^2$ vs r plot was influenced by the loading level and by the shape of the non-adiabatic region, which for each r changed with the θ angle. Also, it was seen that the r_{max} margin was related to the overall data noise levels. No attempts were made to automate the optimization process to define these margins, although mean values of r_{min} and r_{max} were calculated and named R_{min} and R_{max}, respectively. Hence, data points were collected inside the region defined by $2xR_{min}$ and R_{max}. This selected data point location process helped to gather only linear data regions for all 241 θ-angle $1/S^2$ vs r plots. Using this selection process the uncertainty related to locating the crack-tip position (X'_o, Y'_o) ended up being ±3 pixels or less if values of $1.8\times R_{min}$ and $0.9xR_{max}$ were used instead of $2xR_{min}$ and R_{max}. It will be shown in the next sections that the major variable to influence the SIF range determination and the crack tip location is the crack length: shorter crack lengths generating larger errors, and longer crack lengths generating smaller errors.

Stress Intensity Factor Algorithm – Error Function Construction and Minimization

After determining which data points can be fitted by the model, an error function (e) is constructed:

$$e = \sum_{Data\ points} [S - We(x,y)]^2 \tag{7}$$

where e is the error function to be minimized, S is the TSA signal of the point, and We(x,y) is defined by eq. 3.

For the linear approach, the minimization process uses a Least Squares method (LSM) algorithm, and for the non-linear approach, it uses a Downhill Simplex method (Nelder-Mead) [24]. The main advantage of this method is that it does not require differentiation of the data, making it more robust for high gradient problems, such as the crack-tip stress field.

Stress Intensity Factor Algorithm – SIF Calculation and Real Crack Tip Location

After having calculated all the coefficients, the SIF can be calculated as:

$$\Delta K_1 = A_0 A \sqrt{2\pi SR} \tag{8}$$

where ΔK_I is the mode I SIF range in MPa√m, A_0 is the first coefficient as described in eq. 4, A is the TSA calibration

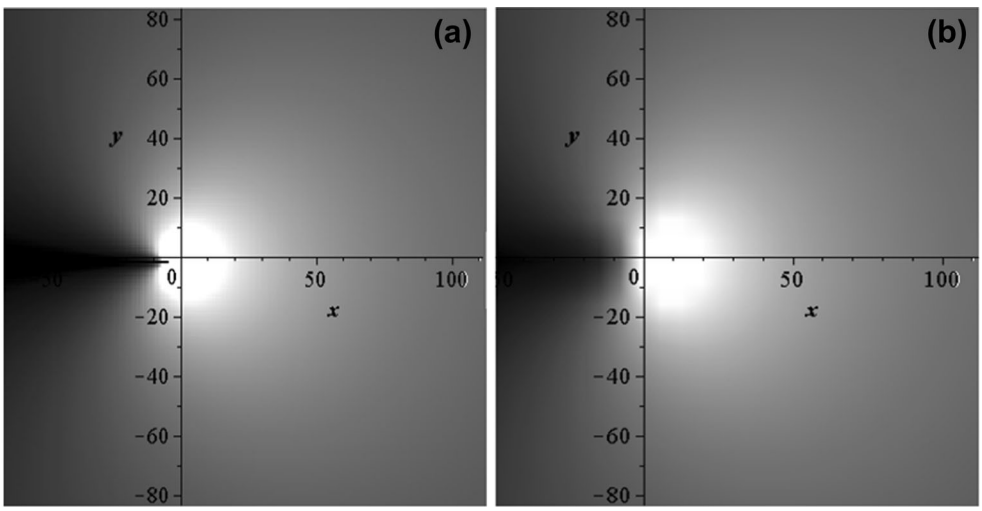

Fig. 7 (**a**) Numerically generated TSA data. (**b**) Calculated model. Crack position (x,y) given in pixels

factor, and SR is the spatial resolution.

In the non-linear approach, the values of x_o and y_o, as seen in eq. 5, are determined, as well as the real location of the crack tip:

$$X_o = X_o^{'} - x_o \qquad Y_o = Y_o^{'} - y_o \tag{9}$$

where X_o and Y_o give the calculated actual position of the crack tip.

Stress Intensity Factor Algorithm – Validation

First, the algorithm is tested using an emulation of TSA data. As an example, Fig. 7(a) shows the numerically generated data, with the crack tip located at (−3,-1) pixels. Figure 7(b) shows the fitted model after a manual crack tip estimation at (−6,-1) pixels.

For the linear approach, where the real crack tip location error is not determined, the result of ΔK_I for short crack lengths was heavily dependent on the crack tip horizontal position estimation (X_o'). As an example, for cracks as short as 3 mm errors up to 10% in ΔK_I occurred for inaccuracies of 1 to 3 pixels in the estimation. For the vertical direction, the dependence was much smaller - a 1 pixel inaccuracy in Y_o' resulted in an error of 0.4% for ΔKI.

The non-linear approach, on the other hand, was able to determine correctly the crack-tip location even for initial crack-tip estimation coordinate (X_o' and Y_o') errors of 20+ pixels in the horizontal and vertical directions; consequently, it gave on-point results for ΔK_I.

After the numerical validation, the SIF determination algorithms were put to the test on actual cracks of different lengths. Table 1 and Fig. 8 show the results obtained for ΔK_I of 8 different crack lengths, using the linear and the non-linear versions of the algorithm as well as results for DIC measurements and FEM simulations [1].

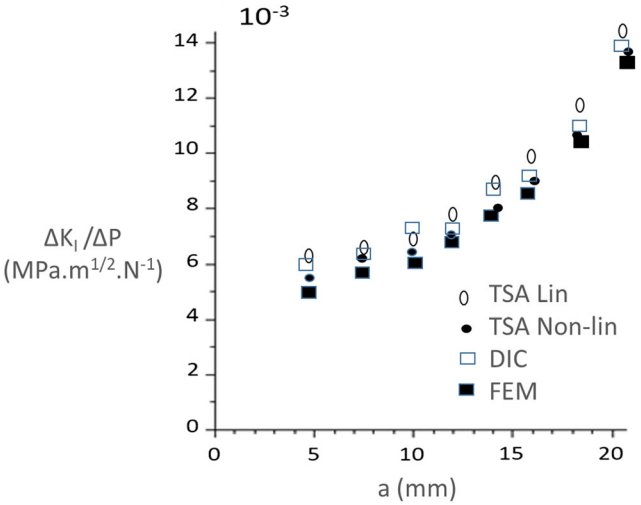

Fig. 8 SIF results for eight different crack lengths

The DIC measurements were conducted on the same specimen used for the TSA measurements. For each of the 8 different crack lengths the DIC ΔK_I finding algorithm used the maximum load applied in the TSA experiments. The VIC-Snap and VIC-3D software programs from Correlated Solutions Inc. (Columbia, SC, USA) were used. DIC data analysis was carried out with a pixel size of 12 μm, with subset, step size and strain window equal to 35, 7 and 7 pixels, respectively. Algorithms similar to those described earlier for the TSA experiments were used to determine crack tip positions and ΔK_I stress intensity factor ranges.

The finite element method (FEM) employed the ANSYS Workbench 15.0 software program. First, before the introduction of a crack, stress concentration factors K_t were determined along the thickness of the keyhole specimen using a 3D model. The 3D model was constructed with tetrahedral solid element SOLID186, which performs better when used in regular meshes, most of them concentrated near the notch root. Fourteen layers of elements were used along the specimen thickness. Due to the model symmetry the linear finite

Table 1 SIF results for eight different crack lengths

a (mm)	ΔP (N)	$\Delta K_I/\Delta P$ TSA Linear 10^{-3} MPa.m$^{1/2}$/N	$\Delta K_I/\Delta P$ TSA Non-linear 10^{-3} MPa.m$^{1/2}$/N	$\Delta K_I/\Delta P$ DIC 10^{-3} MPa.m$^{1/2}$/N	$\Delta K_I/\Delta P$ FEM 3D 10^{-3} MPa.m$^{1/2}$/N
4.7	194	5.98	5.46	5.93	4.99
7.4	196	6.63	6.22	6.71	5.55
10	175	7.02	6.51	7.30	6.10
11.9	161	7.76	7.14	7.57	6.66
14.1	153	9.15	8.04	8.81	7.59
15.9	150	9.80	8.80	9.25	8.64
18.4	145	11.72	10.76	10.96	10.67
20.7	137	14.38	13.43	13.40	13.28

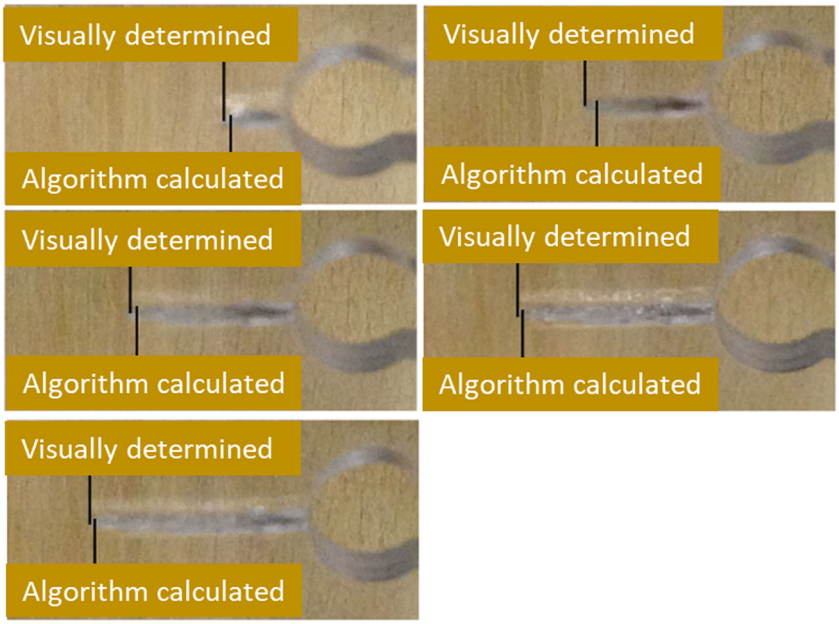

Fig. 9 Photos of the propagating crack

element analysis was run using ¼ of the model. The stress concentration was defined by the ratio of maximum stress and nominal (net) stress. The maximum stress occurred at the keyhole notch root. The stress concentration factor varied monotonically from 3.02 (specimen surface) to 3.17 (point located at half thickness). This variation was expected due to thickness and differences caused by plane stress and plane strain constraint effects. It is important to note that this variation has to be taken into consideration when comparisons are made between results obtained from different experimental and numerical methods such as TSA, DIC, 2D–FEM and 3D–FEM.

The FEM evaluation of ΔK_I for 8 different crack lengths was performed using the ANSYS Workbench fracture tool [1]. The pre-meshed cracked option was used to model the crack, and in this case full model geometry was used. A maximum load of 100 N was used in all analyses. A total of 44,864 SOLID186 type elements were used. Sixteen layers were used along the model's thickness. The thickness effect made the SIF vary along the thickness just as it did with the K_t variation. The ratio between maximum and minimum K_I values was 15% for the specimen with crack length a = 10 mm. Results for the different crack lengths presented in the last column of Table 1 to be compared with the TSA and DIC results correspond to the surface FEM 3D determinations of $\Delta K_I/P$.

The results show that the SIF measurements are very accurate for the non-linear TSA algorithm. Both DIC and TSA (non-linear) results approach the FEM result for longer cracks, because both these calculations are able to locate the real crack tip through optimization, and with longer cracks this process becomes easier and more accurate. Another possible reason why the algorithm gives better results for longer cracks has to do with the fact that the actual crack front is parabolic and the relative error in the crack position diminishes with increasing crack length. The inaccuracy found with the linear TSA algorithm can be attributed to an error in the crack-tip position estimation. Because of the better capability of locating the real crack tip position, the non-linear TSA method is best suited for investigating crack propagation.

Crack Tip Location and Crack Propagation Rate

Before using the SIF algorithm to investigate fatigue crack propagation, it is important to assess its accuracy when locating the crack tip position. This was done by comparing the crack position obtained from the algorithm with the crack size measured using an optical camera. Care was taken so that the camera would take photos simultaneously with the TSA data collection. Figure 9 and Table 2 show the photos and the lengths of a propagating crack. In Fig. 9 the visually-determined and the algorithm-calculated crack tip positions

Table 2 Measured crack lengths and algorithm error

Measured Crack Length (mm)	Measured Crack Tip position (Pixels)	Algorithm Crack Tip Position (Pixels)	Algorithm Crack Length (mm)	Error (mm - %)
4.5	261	265	3.7	0.8–17.8
8.3	268	273	7.3	1.0–12.0
11.1	278	281	10.5	0.6–5.4
13.0	292	293	12.8	0.2–1.5
14.4	311	313	14.0	0.4–2.8

are shown in the images. Table 2 presents measured and algorithm crack lengths as well their differences in milimeters and in percentages. Values in milimeters are presented to call attention to the fact that small differences in length can generate large percentage errors when crack lengths are short. Table 2 also presents columns with crack tip positions given in pixels with the objective of showing the small error (1 to 5 pixels) of crack tip location if measured in terms of pixels.

The results show that the algorithm is sufficiently accurate when finding the real crack tip position. As predicted from the SIF results shown in the last section, as the crack propagates the error diminishes because the stresses are higher and the signal to noise ratio in TSA increases. Some error might be attributed to the fact that the visual localization of the crack tip usually yields a result at the middle of the crack front (notice that the cracks have a parabolic front, not a straight one), whereas the TSA data measures the temperature, and hence the stresses, at the surface of the specimen.

Using the result from the crack tip location, found by the non-linear TSA SIF algorithm, it is easy to calculate the crack propagation rate by dividing the length the crack has grown by the number of cycles between TSA data points (yielding da/dN).

Thermographic Crack Propagation Rate Determination

A second method for measuring the crack propagation rate was developed by combining temperature measurements at fatigue-damaged points near the crack front with an extension of the so-called Risitano's method (or Thermographic method). Risitano's method [20, 21] is used to measure fatigue limit and S-N (Stress vs Number of cycles to failure) curves using an energy damage parameter Φ, which is calculated as the integral of the point-temperature vs cycles plot.

The temperature of some selected points ahead of the crack tip in a specimen with a propagating crack (load range = 170 N with R = 0.35) and a reference temperature were measured during propagation, as seen in Fig. 10.

Figure 11(a) shows the resulting ΔT (temperature at each point minus the reference temperature, taken from an unloaded polycarbonate specimen placed beside the loaded one) vs number of cycles plotted for the eleven points shown in Fig. 10. Each plot is identified by its peak, depicted by a circle mark and by the point number. Figure 11(b) shows the integrated area, related to the parameter Φ, for points 3, 6 and 10.

Table 3 shows the values of Φ obtained for each point after integrating the curves, as shown in Fig. 11(b).

Excluding the two first points, which were already too close to the pre-crack tip at the beginning of the integration process, and which had already accumulated some damage, all the other points show similar results for the damage parameter (coefficient of variation 7.6%). These results suggest a possible way to predict crack paths in real time using temperature measurements and real-time integration of the damage parameter.

The fact that as the crack propagated (for higher N values), the peak temperature increased (although this was predictable

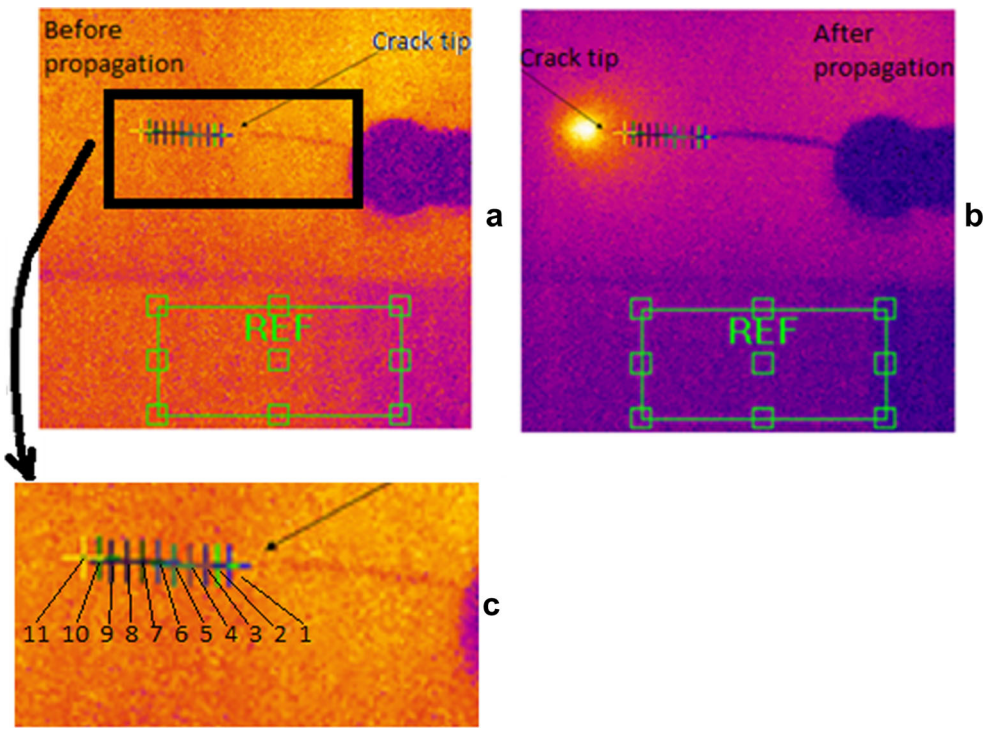

Fig. 10 (**a**) Temperature map and the 11 selected points along the crack path before the propagation. (**b**) Temperature map and the 11 selected points along the crack path after the propagation. (**c**) Zoomed in detail from **a**, numbering the temperature measurement points

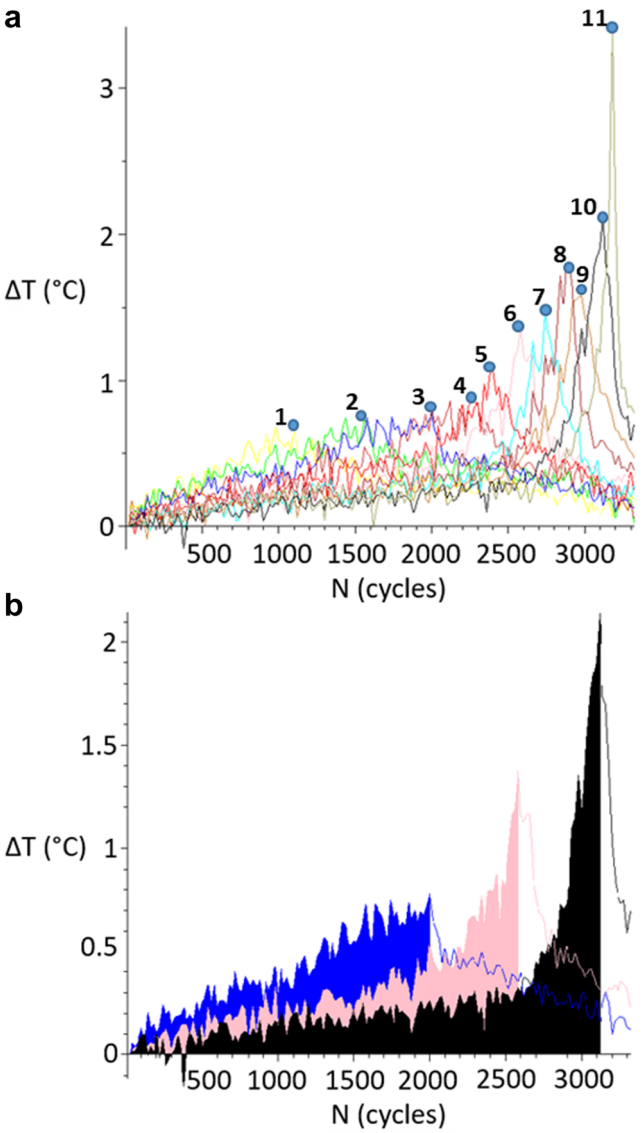

Fig. 11 (**a**) ΔT vs N plots for the 11 points along the crack path. Numbered circle-marks depict the peak of each ΔT-N plot. (**b**) Integration process for Φ determination (example for points 3, 6 and 10)

since the stresses acting at the crack tip also increased), did raise the question of a possible relationship between the temperature variation and the crack growth rate. Both values presented the same exponential growth, characteristic of a non-linear snowball effect (crack propagates faster → stress increases → temperature increases → crack propagates even faster → …). In order to verify this relationship, the same setup used previously with the regular optical camera, was used to measure the crack propagation rate of the fatigue crack shown in Fig. 10. For comparison, the ΔT_{max} (the maximum temperature variation at the measured surface, located at the crack tip) vs the number of cycles plot was recorded.

Figure 12 shows the comparison between these two results. The ΔT_{max} was scaled using the ΔP (load range). As expected, the $\Delta T_{max}/\Delta P$ vs N plot is similar to the plot that would be obtained if the peaks of each of the eleven points shown in Fig. 8 were connected. The results show that there is a clear correlation between the temperature variation and the crack growth rate. This finding proves to be very interesting, since, by using this method, a crack can potentially be monitored in real time, without the need for stress or strain measurements.

Table 3 Damage parameter (Φ) for the 11 points along the crack path

Point	1	2	3	4	5	6
Φ	322.9	533.3	794.8	738.9	837.9	808.4
Point	7	8	9	10	11	
Φ	747	833.2	888.9	862	843.6	

Results and Discussion

In this section, combinations and comparisons between the methods of measuring both da/dN and ΔK, described earlier, are used in order to obtain Paris' law curves that can be compared to values found in the literature. Table 4 summarizes the measurement methods and their combinations that were used to determine the data points present in Figs. 13, 14, 15 and 16. It also mentions results found in the literature regarding non-annealed polycarbonate.

The first experiment consisted of a crack being propagated with ΔP = 225 N and R = 0.3. The pre-crack had a length of 4.2 mm and ended up being 10.5 mm long. Fig. 13 shows the comparison between two methods of measuring da/dN (optical camera and non-linear TSA algorithm), while the values of ΔK were all measured using the SIF-TSA algorithm.

This result clearly shows the interchangeability between the two da/dN measuring techniques, proving that the non-linear TSA algorithm can be self-sufficient when measuring crack propagation curves.

The second experiment consisted of a crack being propagated with ΔP = 160 N and R = 0.27. The pre-crack had a length of 10.4 mm and ended up being 26.6 mm long. Figure 14 shows the comparison between results obtained from the non-linear TSA algorithm and simulations performed using three-dimensional FEM.

The TSA points in the graph were taken from the algorithm (using $2xR_{min}$ in order to leave any crack closure effects out of the problem, since the FEM analysis was not able to predict them). It can be seen that TSA points agreed well with the results obtained in FEM simulation, showing that if the points near the crack tip are ignored, the algorithm can determine the theoretical SIF value. Since the plastic zone around the crack tip is not that big, the stress distribution far from it is not affected by crack closure.

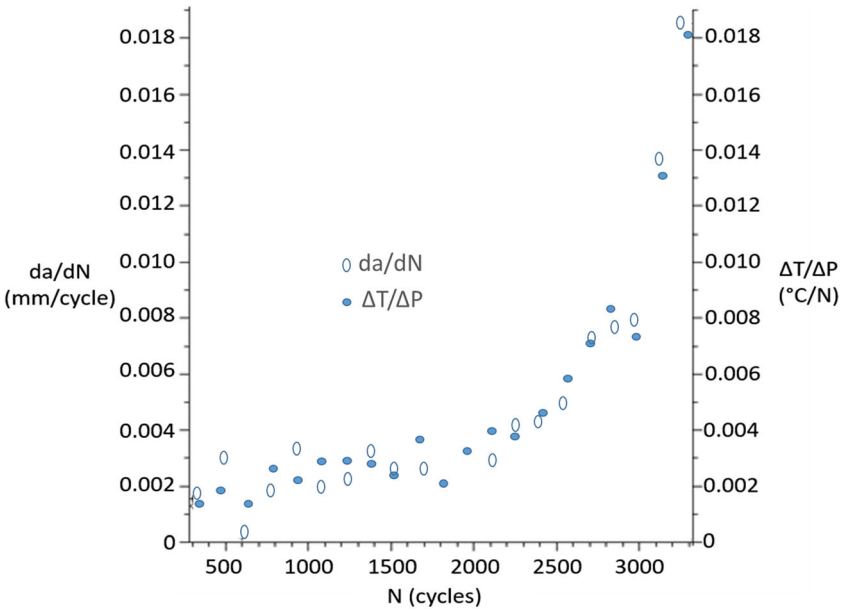

Fig. 12 Comparison between da/dN vs N and $\Delta T_{max}/\Delta P$ vs N

The third experiment consisted of a crack being propagated with $\Delta P = 225$ N and $R = 0.3$. The pre-crack had a length of 12.5 mm and ended up being 20 mm long. Fig. 15 shows the comparison between two da/dN measuring methods (optical camera and temperature measurement). The ΔK values were determined using the FEM simulation, for this test only.

This result illustrates the possibility of measuring crack growth rate using the temperature variation ahead of a crack.

For all results shown in Figs. 13, 14 and 15, the spread for shorter cracks tends to be higher than that for longer cracks. As stated above, this is because, with a constant loading range, the longer the crack, the higher the stresses acting around its

Table 4 Summary of experimental data

Measurement of a and/or da/dN			ΔK determination		Test characteristics		Summary of data in Figs. 13 to 16
Optical	TSA non-linear crack-tip localization algorithm	da/dN via t emperature measurements dT/dP	ΔK via TSA	ΔK via FEM	Present paper, R ratio = 0.27 to 0.3, Key-hole specimen, Frequency = 5 Hz, Temperature = 25 °C Annealed PC Thickness = 3.9 mm Paris constants (mm/cycle, MPa.m$^{1/2}$)		
					C	m	
X			X		1×10^{-3}	2.75	Figure 13
	X		X		9×10^{-4}	2.95	Figure 13
	X			X	1.6×10^{-4}	3.51	Figure 14
	X		X		1.2×10^{-4}	3.76	Figure 14
X				X	9.7×10^{-4}	2.60	Figure 15
		X		X	1.1×10^{-3}	2.42	Figure 15
All (above - present paper) data considered					5×10^{-3}	3.0	Figure 16
Results from Martin and Gerberich [15], SEN specimen, Frequency = 1 Hz, Temperature = 25 °C, Lexan PC non-annealed, Thickness = 6.35 mm, Paris constants C = 2.7×10^{-4}, m = 3.9							Figure 16
Results from Pruitt and Rondinone [18], CTS specimen, R ratio = 0.4, Frequency = 5 Hz, Temperature = 22 °C, Lexan PC non-annealed, Thickness = 2.2 mm, Paris constants C = 2.8×10^{-4}, m = 3.6							Figure 16

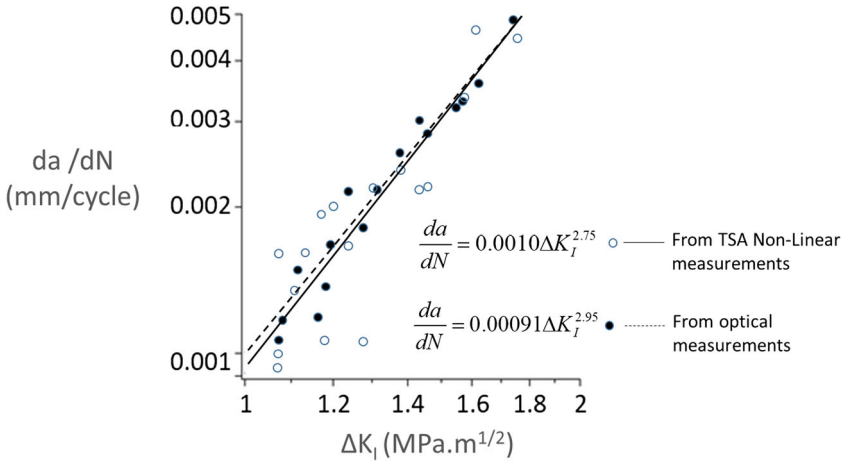

Fig. 13 da/dN vs ΔK curves for two da/dN measuring methods (ΔK from algorithm)

tip, and consequently, the higher the temperature variation that occurs, minimizing the noise to signal ratio of the effective measurements being made during the tests.

Table 4 summarizes the experimental results presented in Figs. 13, 14, 15 and 16. It also presents results from Gerberich et al. [15] and Pruitt et al. for non-annealed polycarbonate. Figure 16 presents a summary of the data presented in the plots of Figs. 13, 14 and 15. Since all experimental data were taken from the key-hole specimens fabricated from the same polycarbonate sheet, with similar loading conditions and at similar ambient temperatures (25 °C), they can be all put in a single graph and a single tendency line can be fitted. Thus Fig. 16 shows the tendency line encompassing all six of the plots generated from the three different data sets, each from a different experiment, as presented in Figs. 13, 14, and 15. Two parallel lines were also added to the tendency line, defining a region between two times faster or two times slower propagation rates. Added to them are the two sets of results found in the literature. In their experiments Gerberich et al. [15] used single edge notch (SEN) specimens with dimensions measuring 50.8 mm by 152.4 mm and 50.8 mm by 203.2 mm with thickness = 6.35 mm, loaded cyclically with 1 Hz at 25 °C. Pruitt et al. [18] used compact tension (CT) specimens with length L = 19 mm, width measured from the center of holes W = 15 mm, height 2H = 19 mm, notch length a_o = 5.33 mm and thickness = 2.2 mm, loaded cyclically with 5 Hz and R = 0.4.

Some variability of the data presented in Figs. 13, 14, 15 and 16 could be explained by the mean load dependence of fatigue crack propagation in polycarbonate, which was reported previously by other authors [18, 19], by ambient temperature variations (temperature variation in the order of 10-20 °C have been reported to cause non negligible effects on fatigue crack propagation in polycarbonate [15]), different specimen thicknesses and also by the residual stresses present in non-annealed specimens. Nonetheless, the results show reasonable agreement, once they fit inside the region defined by twice-as-fast and half-as-slow propagation rates. Consequently, it is possible to see how powerful thermography can be in studying fatigue crack propagation, especially due to its real-time measurements potential.

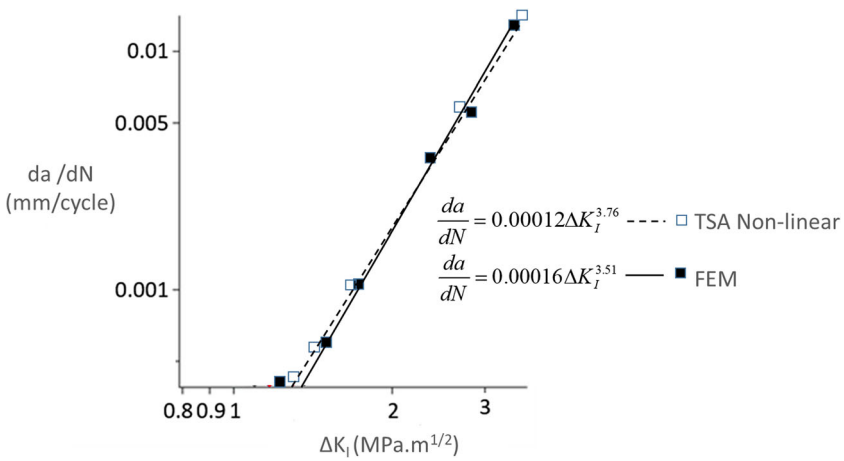

Fig. 14 Measured and simulated da/dN vs ΔK curves

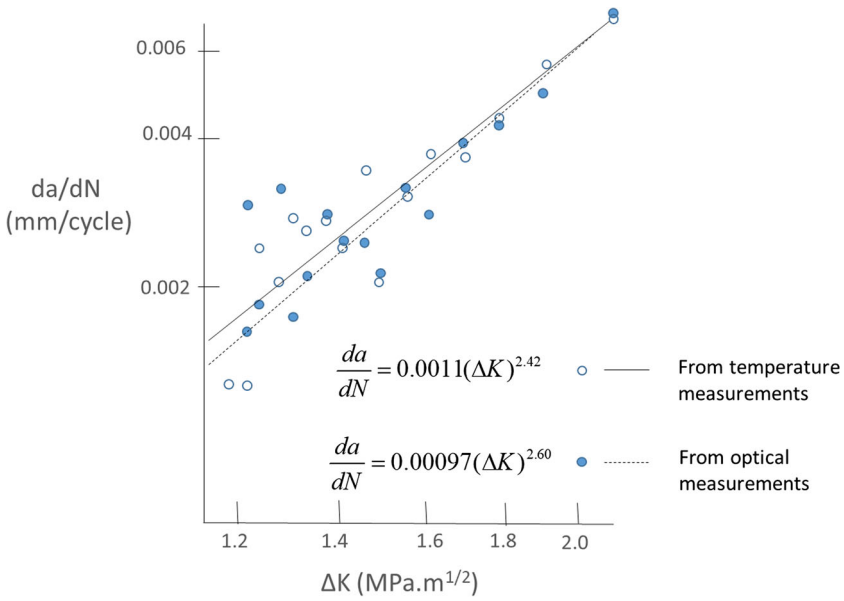

Fig 15 da/dN vs ΔK curves for two da/dN measuring methods (ΔK from FEM)

Conclusions

The experiments described in this paper were easy to set up and used an inexpensive combination of hardware (micro-bolometer camera) and novel software (lock-in and crack tip location) algorithm solutions, which enabled reliable crack growth rate and stress intensity factor measurements. The results presented good agreement with one another and with data found in the literature, making it possible to conclude:

- TSA is a very reliable technique for SIF measurements in polycarbonate.
- The crack tip location and crack growth rate can be determined simultaneously with the SIF determination by using TSA data.

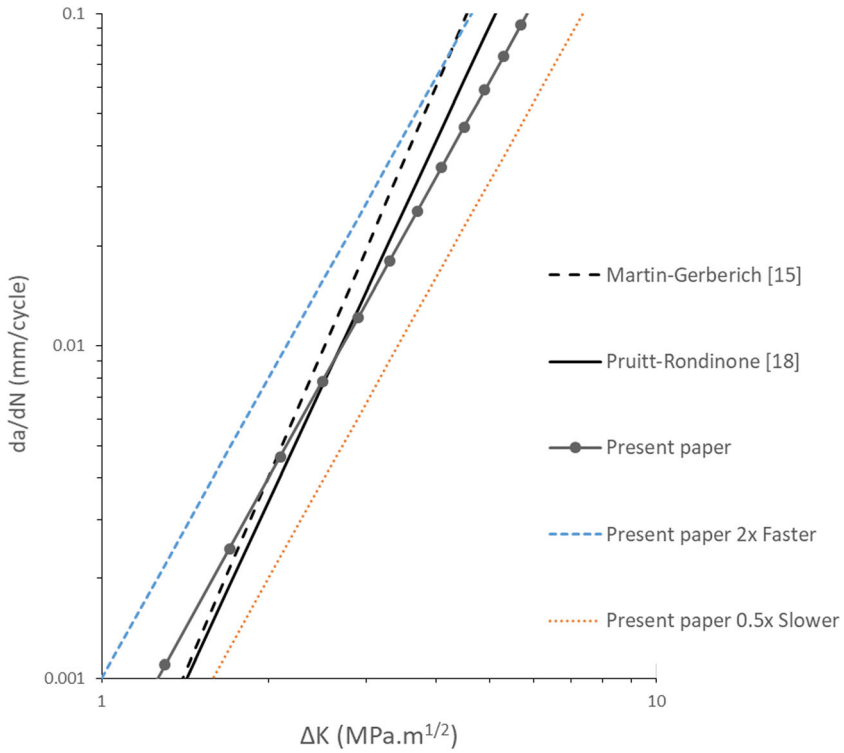

Fig. 16 Comparison between the present paper measured da/dN vs ΔK results and values found in the literature

- Raw temperature measurement near the crack tip directly relates to crack growth rate.
- Infrared thermography can single-handedly measure all necessary parameters for fracture mechanics analysis on the macro-scale.

The two methods used to measure da/dN proved reliable and have a lot of potential for future research, especially the temperature method, which is a very straightforward way of measuring the crack growth rate by means of a very fundamental relationship between the rise in temperature, the rise in stresses, and the speed at which the crack grows. Although different results could be possible for other materials, this relationship seems to be fundamental enough to assume that it will always be present.

Future work will be done concerning the automation of the process, in order to explore the real-time capability of the method. The idea of applying the Risitano damage parameter to crack propagation and the idea of exploring the relationship between da/dN and temperature variation in other materials will also be addressed in the future.

Acknowledgments The research and experiments described in this paper were conducted as part of R.B. Vieira's MSc thesis research at the Pontifical University of Rio de Janeiro (PUC-Rio), with grants from *Conselho Nacional de Desenvolvimento Científico e Tecnológico* and *Fundação de Amparo à Pesquisa do Estado do Rio de Janeiro – FAPERJ.* Authors are grateful to Mr. V.E.L. Paiva, Dr. G.L.G Gonzáles and Prof. R.D. Vieira for suggestions and help with the experiments.

References

1. Vieira RB (2016) Thermography Applied to the Study of Fatigue in Polycarbonate (Master's Thesis). Retrieved from: http://www2.dbd.puc-rio.br/pergamum/tesesabertas/1412756_2016_completo.pdf
2. Vieira RB, González GLG, Freire JLF (2017) Determining Stress Intensity Factors Using Hybrid Thermoelastic Analysis. In: Conference Proceedings of the Society for Experimental Mechanics Series, 1st edn. Springer International Publishing, Orlando, v. 9, p 37–45
3. Dulieu-Barton JM (1999) Introduction to thermoelastic stress analysis. Strain 35(2):35–39
4. Dulieu-Smith SM (1995) Alternative calibration techniques for quantitative thermoelastic stress analysis. Strain 31(1):9–16
5. Stanley P, Chan WK (1986) The determination of stress intensity factors and crack tip velocities from thermoelastic infra-red emissions. In: Proceedings of International Conference of Fatigue of Engineering Materials and Structures, c262, IMechE, Sheffield, UK, pp. 105–114
6. Stanley P, Dulieu-Smith JM (1993) Progress in the thermoelastic evaluation of mixed mode stress intensity factors. In: Proceedings of the SEM Spring Conference on Experimental Mechanics, Dearborn, pp. 617–626
7. Lesniak JR, Bazile DJ, Boyce BR, Zickel MJ, Cramer KE, Welch CS (1997) Stress intensity measurement via infrared focal plane array. Non-Traditional Methods of Sensing Stress, Strain, and Damage in Materials and Structures. ASTM STP 1318, Philadelphia
8. Lin ST, Feng Z, Rowlands RE (1997) Thermoelastic determination of stress intensity factors in orthotropic composites using the J-integral. Eng Fract Mech 56:579–592
9. Tomlinson RA, Nurse AD, Patterson EA (1997) "On determining stress intensity factors for mixed mode cracks from thermoelastic data," Fatigue and Fracture of Engineering. Mater Struct 20:217–226
10. Díaz FA, Yates JR, Tomlinson RA, Patterson EA (2002) Some observation on the application of thermoelasticity to fatigue cracks. In: Proceedings of SEM Annual Conference on Experimental and Applied Mechanics, Milwaukee
11. Díaz FA, Patterson EA, Tomlinson RA, Yates JR (2004) "Measuring stress intensity factors during fatigue crack growth using thermoelasticity," Fatigue and Fracture of Engineering. Mater Struct 27:571–583
12. Marsavina L, Tomlinson RA, Patterson EA, Yates JR (2006) Investigation of crack closure by using thermoelastic stress analysis. In: Proceedings of the 16th European Conference of Fracture, Alexandropoulos, Greece
13. Tomlinson RA, Olden EJ (1999) Thermoelasticity for the analysis of crack tip stress fields – a review. Strain 35(2):49–55
14. Hertzberg RW, Nordberg H, Manson JA (1970) Fatigue Crack Propagation in Polymeric Materials. J Mater Sci 5:521–526
15. Martin GC, Gerberich WW (1976) Temperature effects on fatigue crack growth in polycarbonate. J Mater Sci 11:231–238
16. Hertzberg RW, Manson JA (1980) Fatigue of Engineering Plastics. Academic Press, New York
17. Pitman G, Ward IM (1980) The molecular weight dependence of fatigue crack propagation in polycarbonate. J Mater Sci 15:635–645
18. Pruitt L, Rondinone D (1996) The effect of specimen thickness and stress ratio on the fatigue behavior of polycarbonate. Polym Eng Sci 36(9):1300–1305
19. Haddaoui N, Chudnovsky A, Moet A (1986) Ductile fatigue crack propagation in polycarbonate. Polymer 27:1377–1384
20. Fargione G, Geraci A, La Rosa G, Risitano A (2002) Rapid determination of the fatigue curve by the thermographic method. Int J Fatigue 24:11–19
21. La Rosa G, Risitano A (2000) Thermographic methodology for rapid determination of the fatigue limit of materials and mechanical components. Int J Fatigue 22:65–73
22. Rajik N, Rowlands D (2013) Thermoelastic stress analysis with a compact low-cost microbolometer system. Quant Infrared Thermogr J 10(2):135–158
23. Crawford RJ (1990) Plastics Engineering, 2nd edn. Pergamon Press, New York
24. Nelder JA, Mead R (1965) A simplex method for function minimization. Comput J 7:308–313